Chinese Chemical Letters 34 (2023) 107810

Contents lists available at ScienceDirect

Chinese Chemical Letters

journal homepage: www.elsevier.com/locate/cclet

High-valance molybdenum doped Co_3O_4 nanowires: Origin of the superior activity for 5-hydroxymethyl-furfural oxidation

Bingying Xia[a,1], Guangjin Wang[b,1], Shasha Cui[a], Jinyu Guo[a], Hong Xu[a], Zhijuan Liu[a,*], Shuang-Quan Zang[a,*]

[a] Henan Key Laboratory of Crystalline Molecular Functional Materials, Henan International Joint Laboratory of Tumor Theranostical Cluster Materials, Green Catalysis Center, and College of Chemistry, Zhengzhou University, Zhengzhou 450001, China
[b] School of Materials Science and Energy Engineering, Foshan University, Foshan 528000, China

ARTICLE INFO

Article history:
Received 6 July 2022
Revised 20 August 2022
Accepted 6 September 2022
Available online 10 September 2022

Keywords:
Spinel Co_3O_4
High-valance Mo^{6+}-doping
Electronic structure
Adsorption ability
5-Hydroxymethyl-furfural oxidation

ABSTRACT

Co_3O_4 has been widely explored in electrocatalytic 5-hydroxymethyl-furfural (HMF) oxidation. However, the poor intrinsic ability has seriously limited its electrochemical ability. Heteroatom-doping is an efficient method to enhance the electrocatalytic ability of catalyst by regulating electronic structure. Herein, we have modulated the electronic structure of Co_3O_4 by high valance Mo^{6+}-doping. With the introduction of Mo^{6+}, the content of Co^{2+} was increased and metal-oxygen bond was strength. Electrochemical results suggested that the electrocatalytic ability of Co_3O_4 towards HMF oxidation has been dramatically improved and reaction kinetics has been fasten. Theoretical calculations demonstrated that the surrounding cobalt sites after Mo^{6+}-doping with assembled electron has a strong adsorption ability towards HMF molecule leading to more favourable oxidation of HMF. Post characterizations demonstrated pristine Co_3O_4 structure was kept after electrolysis cycles and CoOOH active species were formed. This work provides a valuable reference for developing efficient heteroatom-doped electrocatalysts for HMF oxidation.

With the increasing expand of world population and rapid consumption of global fossil fuels, energy crisis and environmental issues are serious [1]. Hydrogen has aroused researchers' much attention because of its high energy density and no-pollution. Electrochemical water splitting is an efficient technology to produce hydrogen [2]. However, the sluggishly anodic oxygen evolution reaction (OER) has seriously hinders its energy efficiency and brings about extra energy loss. Moreover, the production, O_2, is less value and dangerous when mixed with hydrogen [3]. Recently, replacing OER with organics oxidation reaction, which usually processes low overpotential and high value-added products, has catch widespread research interest [4]. 5-Hydroxymethyl-furfural (HMF), which is an important platform chemical and with rich resources, can be converted into various valuable chemicals [5]. Electro-oxidation of HMF can obtain 2,5-furandicarboxylic acid (FDCA), which is the promising candidate to terephthalic acid that commonly used in the manufacture of polymers such as polyester and also an intermediate in the synthesis of other important polymers, fine chemicals, phamaceuticals and pesticides [6–9]. Thus, it is of great importance to develop efficient electrocatalysts for HMF oxidation reaction (HMFOR).

Co_3O_4, which is a typical spinel oxide, has been widely explored as an attractive electrocatalyst for HMFOR owing to its high stability and tunable valance state [10–12]. However, poor electrical conductivity and limited intrinsic ability make its electrochemical ability unsatisfactory. The electrical conductivity can be improved by coupled with conductive substrate such as carbon nanomaterials and Ni foam [13–15]. The strong electron interaction between Co_3O_4 and conductive substrate could facilitate electron transfer leading to enhanced electrochemical capacity [14]. Meanwhile, the intrinsic ability of Co_3O_4 could be enhanced by modulating its electronic structure, which has a significant effect on the affinity of active sites to reaction species [16]. Heteroatom-doping is an effective strategy to regulate the electronic structure of electrocatalyst [17]. The introduction of foreign metal or non-metal element could not only provide extra active sites but also make charge redistribution resulting in optimized binding energy to reaction intermediates [18–20]. For example, Zhang *et al.* have synthesized N-doped Co_3O_4, which exhibited superior electrocatalytic ability for HMFOR. The introduction of N benefited the formation of defects and active sites [21]. Wang *et al.* have decorated Co_3O_4 with

* Corresponding authors.
E-mail addresses: zhijuanliu@zzu.edu.cn (Z. Liu), zangsqzg@zzu.edu.cn (S.-Q. Zang).
[1] These authors contributed equally to this work.

https://doi.org/10.1016/j.cclet.2022.107810
1001-8417/

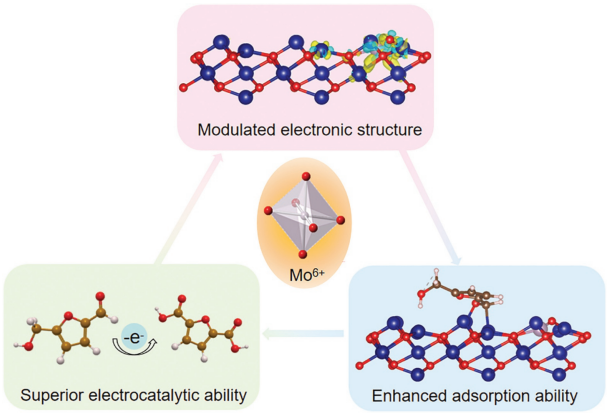

Scheme 1. An illustration about the core relationship between Mo^{6+} doped Co_3O_4, modulated electronic structure, enhanced adsorption ability and its superior electrocatalytic ability towards HMFOR. The blue, pink, red, brown and white balls are represented as Co, Mo, O, C and H, respectively.

single-atom Ir. The introduction of single-atom Ir has enhanced the adsorption with C=C group of HMF resulting in dramatically improved electrocatalytic HMFOR ability [22]. Various 3d transition metal ions such as Fe^{3+}, Ni^{2+} and Cu^{2+} have been doped into Co_3O_4 to tailor its electrochemical ability [23–25]. Moreover, doping with high-valence non-3d transition metal ions such as Zr^{4+}, W^{6+}, Mn^{4+} and Mo^{6+} also is an effective method to enhance the electrochemical ability of Co_3O_4 [20,26-28]. Mo^{6+}, which is a typical high-valence 4d transition metal ion, processed similar ions radius with Co^{3+} and can be used as heteroatoms to replace Co^{3+} in Co_3O_4 [29]. It has been reported that Mo-doping could modulate the electronic property of Co_3O_4 and accelerate charge transfer accounting for superior OER ability [30]. However, the HMFOR electrocatalyst based on Mo-doped Co_3O_4 has not been reported yet. It's of great research value to explore the effects of Mo^{6+}-doping on the electrochemical HMFOR ability of Co_3O_4.

Herein, in this work we have successfully synthesized Mo-doped Co_3O_4 (Mo-Co_3O_4) nanowires to investigate the influence of Mo^{6+}-heteroatoms on electronic structure and electrochemical ability of HMFOR. With the introduction of Mo^{6+}, the Co^{3+} content was decreased and metal-oxygen bond has been strengthened. Electrochemical results demonstrated that Mo-Co_3O_4 exhibited more excellent electrochemical ability with higher current density and lower overpotential than Co_3O_4 for HMFOR. Density functional theory (DFT) revealed that with the introduction of Mo^{6+}, the electron was assembled at surrounding cobalt sites accounting for enhanced adsorption ability with HMF, which results in rich HMF concentration at local active sites (Scheme 1). Post characterization revealed that Mo-Co_3O_4 still kept pristine crystalline structure after four successive electrolysis cycles and displayed good durability. CoOOH species were formed after electrolysis and worked as active sites. This work provides a valuable reference for developing efficient heteroatom-doped electrocatalysts.

Synthesis of Co_3O_4 doped with different Mo content: Ni foam was washed with 2 mol/L HCl, ultra-pure water and ethanol, subsequently, before using. 232.5 mg $Co(NO_3)_2{\cdot}6H_2O$, calculated amount of $Na_2MoO_4{\cdot}2H_2O$ (molar ratio of Co/Mo of 10:0.1, 10:0.5 and 10:1) and 242.4 mg urea were dissolved in 30 mL ultra-pure water with continuously stirring for 30 min. Then, a piece of washed Ni foam (3×4 cm) and the mixture were placed into a 50 mL autoclave and suffered from 393 K for 10 h. After cooling to room temperature, the sample was taken out and washed with ultra-pure water and ethanol followed by drying at 333 K for 2 h. Finally, Mo-doped Co_3O_4 could be obtained by annealing at 623 K for 2 h at a heating rate of 278 K/min. The samples with feeding Co/Mo ratio of 10:0.1, 10:0.5 and 10:1 were named as Mo-Co_3O_4 (10:0.1), Mo-Co_3O_4, and Mo-Co_3O_4 (10:1). Mo-Co_3O_4 was explored in detail.

All the electrochemical measurements including cyclic voltammetry (CV), linear sweep voltammetry (LSV) and constant potential were tested in CHI 760E CH Instrument electrochemical workstation. The samples that grown on Ni foam were cut into 1×1 cm and used as working electrode. The counter electrode and reference electrode were carbon rode and saturated calomel electrode (SCE), respectively. LSV curves were recorded at 5 mV/s. All potentials were referenced to a reversible hydrogen electrode (RHE) according to: $E_{RHE} = E_{SCE} + 0.242 + 0.059 \times pH$. The nyquist plots were measured at the frequency range from 0.01 Hz to 100 kHz.

The morphology of samples were investigated by scanning electron microscopy (SEM, Zeiss Signma 500). Transmission electron microscopy (TEM) images were obtained in JEM-2100. The bulk crystal structure of the obtained samples is characterized using powder X-ray diffraction (XRD, D/MAX-3D diffractometer). X-ray photoelectron spectroscopy (XPS) were tested using ESCALAB 250 system (Thermo Fisher Scientific, England) and were used to explore the electronic structure. BET analysis was performed on Belsorp Max. The Raman spectra were collected on labRAM HR Evolution-HORIBA Raman system. The temperature-programmed desorption in ammonia (NH_3-TPD) was tested in a Micromeritics Autochem II 2920 chemisorption analyzer. The samples were heated up to 423 K at 10 K/min and kept for 30 min in He flow to remove adsorbed impurities. Afterwards, the samples were heated up to 313 K for the adsorption of NH_3. After flushing with He for 1 h, the physically adsorbed NH_3 could be removed. TPD data was recorded from 313 K to 873 K with 10 K/min. The quantify of NH_3 adsorption was calculated by integration of peak area and the adsorption of exhaust NH_3.

High-performance liquid chromatography (HPLC, Shimadzu Prominence LC-2030C system) with an ultraviolet-visible detector was applied to detect and analyze HMF oxidation products. 20 μL of electrolyte was sampling during potentiostatic electrolysis and diluted to 2 mL with ultrapure water and analyzing it by HPLC. The wavelength of the UV detector was set to 265 nm, mobile phase A and phase B was methanol and 5 mmol/L ammonium formate aqueous solution, respectively. The ratio of A:B was 3:7 and flow rate was 0.6 mL/min. A 4.6 mm × 250 mm Ultimate 5 μm AQ-C18 column was used and each separation lasts 10 min.

The HMF conversion, FDCA yield and faradaic efficiency were calculated using the following equations, respectively.

$$\text{HMF conversion } (\%) = [n(\text{HMF consumed})/n(\text{HMF initial})] \times 100 \quad (1)$$

$$\text{FDCA yield } (\%) = [n(\text{FDCA formed})/n(\text{HMF initial})] \times 100 \quad (2)$$

$$\text{Faradaic efficiency } (\%) = [n(\text{FDCA formed})/(\text{Charge}/6F)] \times 100 \quad (3)$$

where F is the Faraday constant (96,485 C/mol) and n is the mol of reactant calculated from the concentration measured by HPLC.

All DFT calculations were performed using Vienna ab initio simulation package (VASP). The interaction between ion and electron was described with the projector-augmented-wave (PAW) method. A 400 eV cut off energy for the plane wave expansion was adopted in all the calculations. Hubbard U correction (DFT+U) was employed using the generalized gradient approximation (GGA) of Perdew–Burke–Ernzerhof (PBE) methods for accounting for the correlation energy of the strongly localized 3d orbital, and setting U-J = 3.5 eV and 2.0 eV for Co and Mo atoms in this work. A vacuum layer of 20 Å was added into two adjacent two consecutive slabs for eliminating their interaction. The total energy and force

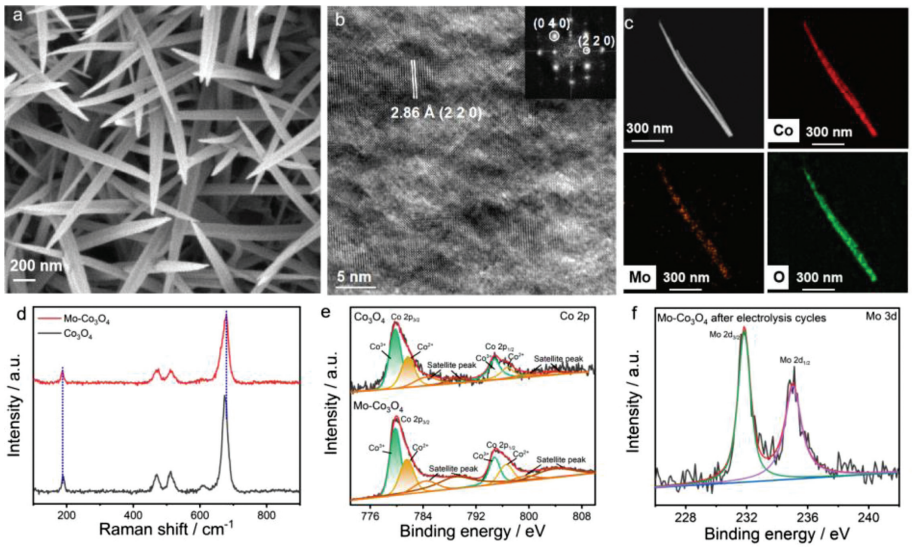

Fig. 1. (a) SEM image, (b) HRTEM image and (c) corresponding element mapping image of Mo-Co_3O_4. (d) Raman spectra of Co_3O_4 and Mo-Co_3O_4. (e) Co 2p XPS spectra of Co_3O_4 and Mo-Co_3O_4. (f) Mo 3d XPS spectra of Mo-Co_3O_4.

convergence criteria were set as 1×10^{-4} eV and 0.02 eV/Å, respectively. In addition, the dipole correction was applied in all slab calculations.

SEM was performed to explore the morphology of Mo-doped Co_3O_4. As shown in Fig. S1a (Supporting information), pure Co_3O_4 was consistent with nanowires. With the introduction of Mo, the nanowires microscopy was still kept and a few nanosheets were appeared when the feeding molar ratio of Co/Mo was 10:1 (Fig. 1a and Fig. S1 in Supporting information). XRD was used to detect the crystalline structure of samples. As shown in Fig. S2 (Supporting information), the doping of Mo-heteroatoms did not change the spinel Co_3O_4 structure. The diameter distribution of Mo-Co_3O_4 nanowires was shown in Fig. S3 (Supporting information). High-resolution TEM (HRTEM) was applied to explore the crystalline structure of Mo-Co_3O_4 at high spatial resolution. In Fig. 1b, the measured lattice fringe of 2.86 Å was attributed to (220) crystal face of Co_3O_4. The inset image was its fast Fourier transform (FFT) image, which can be well indexed to (040) and (220) lattice plane of Co_3O_4. The selected area electron diffraction (SAED) image of Mo-Co_3O_4 was shown in Fig. S4 (Supporting information) and indicated to spinel Co_3O_4 phase. Element mapping images of Mo-Co_3O_4 (Fig. 1c) revealed the uniform distribution of Co, Mo and O, respectively. The atom ratio of Co/Mo in Mo-Co_3O_4 was detected by Energy dispersive spectra (EDS) to be about 37:1 (Table S1 in Supporting information). Inductively coupled plasma-optical emission spectroscopy (ICP-OES) was also used to detect the Co/Mo ratio in Mo-Co_3O_4. As shown in Table S2 (Supporting information), the Co/Mo was to be 31:1, which was close to EDS data. Raman spectra was carried out to investigate the bond vibration mode in Co_3O_4 and Mo-Co_3O_4. It can be clearly seen from Fig. 1d that Co_3O_4 displayed a typical spinel vibration mode. The Raman band at 188.0 and 673.9 cm^{-1} were corresponded to $F^1{}_{2g}$ symmetry of tetrahedral sites and A_{1g} mode of octahedral sites, respectively. The band at 470.5 and 512.6 cm^{-1} were assigned to $F^2{}_{2g}$ and E_g mode owing to the vibration of tetrahedral and octahedral sites, respectively. The weak band at 608.4 cm^{-1} was associated with F_{2g} mode. The Raman band of A_{1g} mode in Mo-Co_3O_4 showed a shift to higher wavenumber compared with pristine Co_3O_4, indicating the screwy octahedron sites owing to the doping of Mo [31]. XPS was used to explore the electronic structure of Co_3O_4 and Mo-Co_3O_4. It can be seen from Fig. S5 (Supporting information) that Mo has been successfully doped into Co_3O_4. For Co 2p XPS spectra (Fig. 1e), it can be divided into eight contributions. The peaks at 779.8, 781.7, 784. 5 and 788.8 eV formed Co $2p_{3/2}$. While Co $2p_{1/2}$ were constituted with four peaks at 794.8, 796.7, 799.5 and 803.8 eV, respectively. The peak at 779.8 and 781.7 eV were assigned to Co^{3+} and Co^{2+}, respectively. The ratio of Co^{3+}/Co^{2+} in Co_3O_4 and Mo-Co_3O_4 was calculated to be about 1.59 and 1.40, respectively. The decreased Co^{3+} content may be owing to the substitution of Co^{3+} at octahedron sites with Mo^{6+} [30]. The ratio of Co^{3+}/Co^{2+} was 1.48 and 1.31 in Mo-Co_3O_4 (10:0.1) and Mo-Co_3O_4 (10:1), respectively (Fig. S6a in Supporting information). The Mo 3d XPS spectra can be deconvoluted into two peaks at 231.9 and 235.1 eV, respectively, which corresponded to Mo^{6+} species (Fig. 1f and Fig. S6b in Supporting information) [30]. For O 1s XPS spectra, it can be divided into three peaks. The peaks at 529.6 and 531.1 eV were attributed lattice oxygen and metal oxyhydroxides, respectively. While, the peak at 533.2 eV was corresponding to adsorbed water species. The O 1s XPS spectra in Mo-Co_3O_4 exhibited a shift towards higher binding energy compared with Co_3O_4, indicating a stronger metal-oxygen interaction (Fig. S7 in Supporting information) [32]. Based on above, the electronic structure of Co_3O_4 has been well modulated with the introduction of Mo^{6+}. Wang *et al.* have reported that the Co^{2+} in Co_3O_4 was responsible for the adsorption of HMF [33,34]. Thus, it can be expected that Mo-Co_3O_4 would exhibited an enhanced adsorption ability and preferable electrochemical ability for HMF oxidation.

The electrochemical abilities of samples were evaluated in a three-electrode system using 1.0 mol/L KOH as electrolyte. The LSV curves with 50 mmol/L HMF and 0 mmol/L HMF were recorded to compare the electrochemical ability of HMFOR with OER. It is clearly seen from Fig. 2a that with the addition of HMF, the current density of both Co_3O_4 and Mo-Co_3O_4 were obviously increased suggesting the preferential oxidation of HMF than OH^-. What is more, the current density of Mo-Co_3O_4 was significantly higher than that of Co_3O_4 at the same overpotential. The electrochemical performance of Co_3O_4 doped with different Mo content was tested to explore its influence on catalytic ability. As shown in Fig. S8 (Supporting information), the electrochemical ability of Co_3O_4 for HMF oxidation has been rapidly improved with the doping of Mo. What's more, Mo-Co_3O_4 displayed the most excellent electrochemical ability. As shown in Fig. 2b that Mo-Co_3O_4 only need 1.39 V to reach 30 mA/cm^2, which was 146 mV smaller than that of Co_3O_4. The current density of Mo-Co_3O_4 was about two

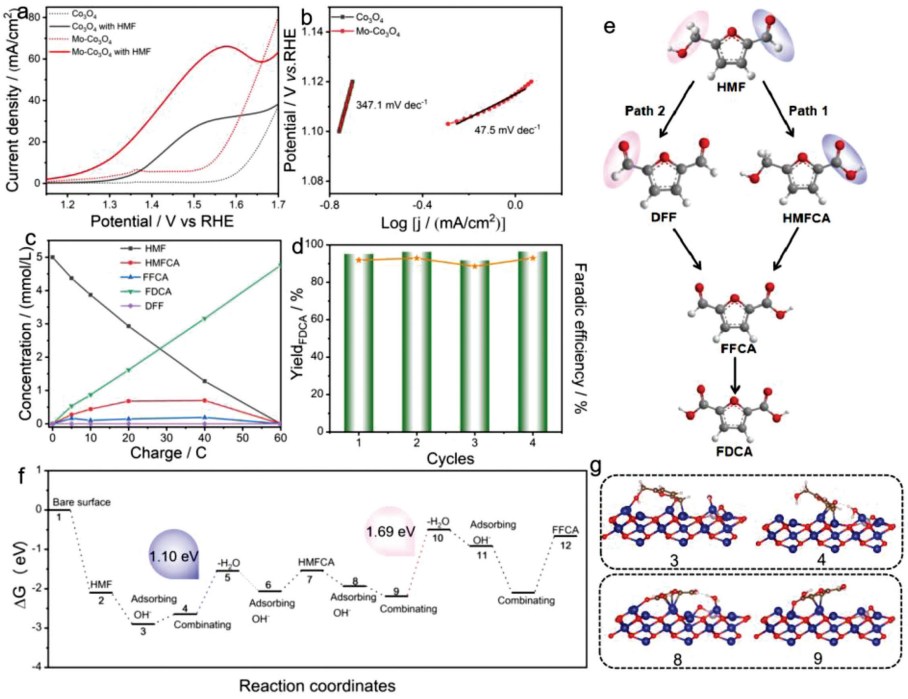

Fig. 2. (a) LSV plots of Co_3O_4 and Mo-Co_3O_4 in 1.0 mol/L KOH with or without 50 mmol/L HMF without iR compensation. (b) The potential at 30 mA/cm^2 and current density at 1.50 V on both Co_3O_4 and Mo-Co_3O_4. (c) The reaction pathway of HMF oxidation; (d) The concentration of DFF, HMFCA, FFCA, FDCA and HMF during HMF oxidation. (e) The yield$_{FDCA}$ (%) and Faradic efficiency (%) of Mo-Co_3O_4 under four successive electrolysis cycles. (f) Reaction free energy barrier for the oxidation of aldehyde and hydroxyl groups on Mo-Co_3O_4. (g) Structure models for the dehydration of hydroxyl and aldehyde oxidation on Mo-Co_3O_4.

times higher than that of Co_3O_4 at 1.50 V indicating the greatly improved electrochemical ability of Co_3O_4 after the introduction of Mo-heteroatoms. The electrocatalytic performance of Mo-Co_3O_4 compared with other HMF electro-oxidation catalysts has been provided in Table S3, which displayed excellent catalytic ability. In order to exclude the influence of the number of exposed active sites on electrochemical ability, the electrochemical active surface areas (ECSA) was calculated according to the electrical double-layer capacitor (C_{dl}). The CV plots of Co_3O_4 and Mo-Co_3O_4 at different scan rates were shown in Fig. S9 (Supporting information), whose C_{dl} were 23.92 and 26.27 mF/cm^2, respectively. After normalized by the ECSA, Mo-Co_3O_4 also exhibited better electrochemical ability than that of Co_3O_4, suggesting the enhanced intrinsic ability (Fig. S10 in Supporting information). HPLC was used to explore the reaction pathway and detect products of HMFOR on Mo-Co_3O_4. In usual, HMF oxidation takes two pathways. In path 1, the aldehyde group of HMF was prior to be oxidized into carboxyl group forming 5-hydromethyl-2-furancarboxylic acid (HMFCA). For path 2, the hydromethyl group was firstly oxidized into aldehyde groups forming 2,5-diformylfuran (DFF). Both HMFCA and DFF can be oxidized into 2-furancarboxylic acid (FFCA). Finally, FDCA could be obtained by the oxidation of FFCA (Fig. 2c) [35]. The potentiostatic electrolysis at 1.40 V in 5 mmol/L HMF was carried out to detect intermediate products of HMF oxidation using Mo-Co_3O_4 electrode. The concentration of HMF, DFF, HMFCA, FFCA and FDCA standard substances was quantified by HPLC (Figs. S11-S15 in Supporting information). As shown in Fig. 2d and Fig. S16 (Supporting information), DFF was hardly to be detected and the concentration of HMFCA was higher, indicating that the dominated pathway of HMF oxidation was path 1. Mo-Co_3O_4 exhibited a high FDCA yield (yield$_{FDCA}$) (95%) and faradaic efficiency (92%). To evaluate the electrochemical stability of Mo-Co_3O_4, four successive electrolysis cycles was performed. In Fig. 2e, the yield$_{FDCA}$ and Faradaic efficiency were almost unchanged, suggesting a good durability of Mo-Co_3O_4. The prior oxidation of aldehyde group on Mo-Co_3O_4 was further evidenced by DFT calculation. The reaction models and reaction free energy were shown in Figs. 2f and g and Fig. S17 (Supporting information). In path 1, both OH^- and HMF are firstly adsorbed on the Mo-Co_3O_4 surface. Then, OH^- was attend to capture H^+ from the aldehyde of HMF to form H_2O. Another OH^- was combined with dehydrated aldehyde to form carboxylic acid. For path 2, the adsorbed OH^- was combined with H^+ of hydroxy to form H_2O following by desorption. As shown in Fig. 2f, the free energy barrier of dehydration of path 2 (1.69 eV) was higher than that of dehydration of path 1 (1.10 eV), suggesting aldehyde was preferential than hydroxymethyl to be oxidized on Mo-Co_3O_4, which was consistent with HPLC results [36].

In order to investigate the adsorption ability of Co_3O_4 and Mo-Co_3O_4, TPD was performed. Since C=O group was rich in electron, the adsorption ability of Lewis acidic sites at NH_3 atmosphere was shown in Fig. S18 (Supporting information) [37]. It can be seen clearly that Mo-Co_3O_4 exhibited higher desorption temperature than Co_3O_4 suggesting the adsorption ability has been strengthen with Mo^{6+}-doping. Open-circuit potential (OCP) was recorded to evaluate the absorb ability in Helmholtz layer [38]. As displayed in Fig. S19 (Supporting information), the OCP of Co_3O_4 was 0.06 V after injecting 50 mmol/L HMF. Mo-Co_3O_4 exhibited a more significant drop of OCP (0.11 V) indicating a strong surface adsorption of HMF. The electrochemical abilities of Co_3O_4 and Mo-Co_3O_4 in furfuraldehyde and furfuryl alcohol were tested to explore the adsorption ability towards different groups of HMF (Fig. S20 in Supporting information). As summarized in Fig. S21 (Supporting information), Mo-Co_3O_4 displayed the promoted oxidation of hydroxymethyl and aldehyde groups simultaneously [39]. What is more, the current density of hydroxymethyl oxidation was increased more obviously than that of aldehyde groups on Mo-Co_3O_4 electrode demonstrating the oxidation of hydroxymethyl seriously limited the oxidation process of HMFOR. With the introduction of Mo-heteroatoms, hydroxymethyl oxidation was accelerated [40]. *In situ* Bode-phase plots was performed to explore the reaction kinet-

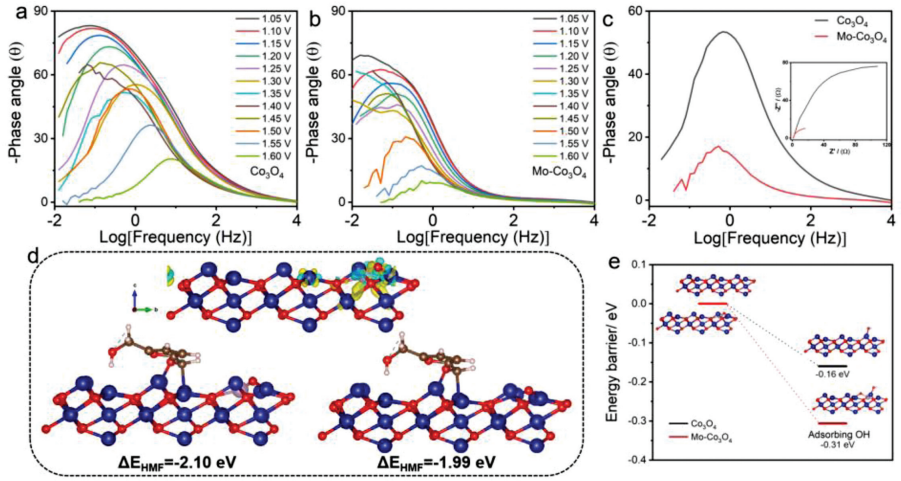

Fig. 3. *In situ* Bode-phase plots of (a) Co_3O_4 and (b) Mo-Co_3O_4 at different potentials in HMF. (c) The Bode-phase plots and Nyquist plots Co_3O_4 and Mo-Co_3O_4 at 1.50 V. (d) Side-view of differential charge density of Mo-Co_3O_4 (top), where the yellow and cyan represent electron accumulation and depletion with an isosurface value of 0.01 e/Å^3, respectively. The calculated adsorption energies and optimized structure of HMF on Mo-Co_3O_4 (left) and Co_3O_4 (right). (e) The energy barrier of OH* adsorption on Co_3O_4 and Mo-Co_3O_4.

ics at electrode/electrolyte interface. It has been widely accepted that the signal at high frequency (10^2–10^3 Hz) was attributed to the electron transfer between electrocatalyst inner and electrode interface while the peak at low frequency (10^{-2}–10^2 Hz) was corresponding to charge transfer during electrocatalytic process [41]. In Fig. 3a, Co_3O_4 displayed a peak at low frequency revealing the electrocatalytic process was dominated by charge transfer. With the increase of potential, the peak became sharper and lower indicating that charge transfer was accelerated. Moreover, the tendency of peak on Co_3O_4 electrode was gently, which may be limited by poor electronic conductivity. For Mo-Co_3O_4 (Fig. 3b), it showed similar signal with Co_3O_4 demonstrating the electrocatalytic process of both Mo-Co_3O_4 and Co_3O_4 was dominated by charge transfer. The tendency of peak was sharp suggesting the electronic conductivity of Co_3O_4 was improved with the doping of Mo-heteroatoms. For comparison, the Bode-angle plots at 1.50 V of Mo-Co_3O_4 and Co_3O_4 were shown in Fig. 3c. It is obvious that the peak of Mo-Co_3O_4 was lower and sharper than that of Co_3O_4 demonstrating that more electrons were participated in electrochemical reaction on Mo-Co_3O_4 electrode [42]. The inset was their corresponding nyquisty plots. The smaller of semicircle diameter, the smaller of charge transfer resistance. It can be clearly found that Mo-Co_3O_4 displayed faster reaction kinetics than Co_3O_4. DFT calculation was carried out to explore the origin of superior electrocatalytic ability towards HMFOR. It has been widely accepted that the electronic structure of electrocatalyst plays a significantly role on the adsorption/desorption with reaction intermediates. The differential charge density of Mo-Co_3O_4 was calculated and shown in Fig. 3d. Due to the introduction of high valance of Mo^{6+}, the electron was transferred from Mo to Co, resulting in assembled charge at surrounding cobalt atom. The Bader charge analysis results showed that the number of electron transferred from Mo to Co was 1.81, which was accordance with the XPS results in Fig. 1e. The modulated electronic structure may have a great effect on adsorption with HMF on Mo-Co_3O_4 electrode [43]. The optimal adsorption structure of HMF molecule on Mo-Co_3O_4 and Co_3O_4 were shown in Fig. 3d. It is clearly can be seen that the adsorption site in both Mo-Co_3O_4 and Co_3O_4 were same. However, the adsorption energy of HMF (ΔE_{HMF}) was −2.10 eV, which was smaller than that of Co_3O_4 (−1.99 eV), which revealed that the adsorption of HMF molecule was more favorable on Mo-Co_3O_4. The enhanced adsorption ability with HMF may result from the modulated electron structure with the introduction of Mo^{6+}. From the electrochemical LSV carves, it can be seen that the current density of HMFOR on Mo-Co_3O_4 electrode was began to increase at 1.15 V, which was smaller than the potential of catalyst oxidation, indicating the HMFOR was a direct oxidation process [36]. It has been reported previously that the adsorption of OH^- plays a crucial role on the reaction kinetics of HMFOR [44]. The free energy barrier of OH^- on Co_3O_4 and Mo-Co_3O_4 was calculated and shown in Fig. 3e. It has been found that Mo-Co_3O_4 can adsorb OH^- much more easily than Co_3O_4. Above all, the reaction kinetic of Co_3O_4 for HMFOR has been accelerated with the introduction of Mo-heteroatoms. The superior electrocatalytic ability was mainly attributed to enhanced adsorption ability towards HMF molecule owing to modulated electronic structure of surrounding cobalt atoms.

Post characterizations of Mo-Co_3O_4 after four successive electrolysis cycles were carried out to explore the evolution of crystalline structure and electronic environment. It can be seen from Fig. S22 (Supporting information) that spinel Co_3O_4 structure was kept after electrolysis cycles. As shown in Fig. S23 (Supporting information), it can be clearly seen that after electrolysis cycles Mo-Co_3O_4 still kept nanowires morphology. As shown in Fig. 4a, the Raman spectra of Mo-Co_3O_4 after four successive electrolysis cycles also displayed a Co_3O_4 vibration mode. HRTEM was performed to index the crystalline structure. The measured lattice fringes of 2.85 and 4.67 Å, corresponding to (220) and (111) crystal face of Co_3O_4, respectively, which was consistent with its FFT image (Fig. 4b inset) along [110] zone axis. XPS was applied to explore the surface valance state of Co and Mo after electrolysis. As shown in Fig. 4c, the ratio of Co^{3+}/Co^{2+} was increased to 1.50 indicating the possible formation of CoOOH active species [21]. For Mo 3d (Fig. 4d), it still was in Mo^{6+} state. The O 1s XPS spectra of Mo-Co_3O_4 after electrolysis cycles was shown in Fig. S24 (Supporting information), it is obvious that the peak intensity at around 531.0 eV, which was attributed to metal oxyhydroxides [34], was relatively higher than that in Mo-Co_3O_4. Above all, Mo-Co_3O_4 still kept its nanowire morphology and spinel Co_3O_4 structure after electrolysis cycles. CoOOH species may formed at surface and worked as active sites for HMF electro-oxidation.

In summary, to further enhance the electrocatalytic HMFOR activity of Co_3O_4, we have doped high-valance Mo^{6+} on its surface to regulate electronic structure and strength absorption ability. With the doping of Mo^{6+}, the content of Co^{3+} has been decreased and interaction of metal-oxygen bond has been strength. Electrochemical results demonstrated that Mo-Co_3O_4 exhibited more out-

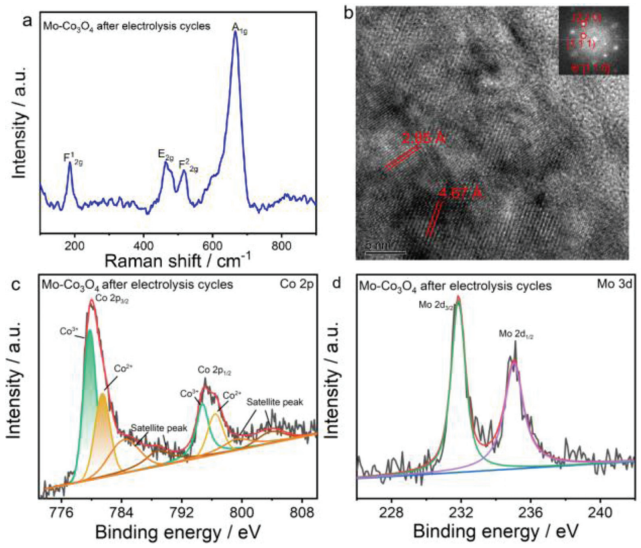

Fig. 4. (a) Raman spectra, (b) HRTEM, (c) Co 2p XPS spectra and (d) Mo 3d XPS spectra of Mo-Co_3O_4 after four successive electrolysis cycles.

standing HMFOR ability and faster reaction kinetics than Co_3O_4. DFT calculations revealed that the electron was assembled at surrounding cobalt site leading to an enhanced adsorb with HMF after Mo^{6+}-doping. Post-characterization demonstrated that Mo-Co_3O_4 after four successive electrolysis cycles was kept its original crystalline structure revealing good structure stability. XPS results proved the formation of CoOOH species, which may work as active sites. This work provides a valuable reference for designing efficient heteroatom-doped electrocatalysts for electrochemical HMFOR.

Declaration of competing interest

The authors declare that they have no known competing financial interests or personal relationships that could have appeared to influence the work reported in this paper.

Acknowledgments

This work was supported by National Natural Science Foundation of China (Nos. 92061201, 21825106, 22102155 and 32072304), the China Postdoctoral Science Foundation (Nos. 2021M692909 and 2022T150587), the Program for Innovative Research Team (in Science and Technology) in Universities of Henan Province and Zhengzhou University (No. 19IRSTHN022) and the Key Scientific and Technological Project of Henan Province (No. 2021102210027).

Supplementary materials

Supplementary material associated with this article can be found, in the online version, at doi:10.1016/j.cclet.2022.107810.

Reference

[1] S. Pacala, R. Socolow, Science 305 (2004) 968–972.
[2] J. Wang, W. Cui, Q. Liu, et al., Adv. Mater. 28 (2016) 215–230.
[3] N. Jiang, B. You, R. Boonstra, et al., ACS Energy Lett. 1 (2016) 386–390.
[4] H. Zhou, Z. Li, L. Ma, H. Duan, Chem. Commun. 58 (2022) 897–907.
[5] C. Xu, E. Paone, D. Rodríguez-Padrón, R. Luque, F. Mauriello, Chem. Soc. Rev. 49 (2020) 4273–4306.
[6] Y. Zhao, M. Cai, J. Xian, Y. Sun, G. Li, J. Mater. Chem. 9 (2021) 20164–20183.
[7] G. Yang, Y. Jiao, H. Yan, et al., Adv. Mater. 32 (2020) 2000455.
[8] Y. Lu, T. Liu, C.L. Dong, et al., Adv. Mater. 34 (2022) 2107185.
[9] M. Lu, M. Zhang, C.G. Liu, et al., Angew. Chem. Int. Ed. 60 (2021) 4864–4871.
[10] M.J. Kang, H. Park, J. Jegal, et al., Appl. Catal. B: Environ. 242 (2019) 85–91.
[11] M. Li, Y. Deng, G. Wu, et al., Aggregate 2 (2021) e17.
[12] H.L. Chen, Q.T. Huang, S.R. Hu, et al., Chin. J. Struct. Chem. 39 (2020) 1035–1043.
[13] X.F. Lu, L.F. Gu, J.W. Wang, et al., Adv. Mater. 29 (2017) 1604437.
[14] X. Yang, H. Li, A.Y. Lu, et al., Nano Energy 25 (2016) 42–50.
[15] L. Xu, Q. Jiang, Z. Xiao, et al., Angew. Chem. Int. Ed. 128 (2016) 5363–5367.
[16] C. Xie, D. Yan, W. Chen, et al., Mater. Today 31 (2019) 47–68.
[17] G. Yang, Y. Jiao, H. Yan, C. Tian, H. Fu, Small Struct. 2 (2021) 2100095.
[18] Y. Wang, M. Qiao, Y. Li, S. Wang, Small 14 (2018) 1800136.
[19] R. Li, Y. Guo, H. Chen, et al., ACS Sustain. Chem. Eng. 7 (2019) 11901–11910.
[20] S.L. Zhang, B.Y. Guan, X.F. Lu, et al., Adv. Mater. 32 (2020) 2002235.
[21] M. Sun, Y. Wang, C. Sun, et al., Chin. Chem. Lett. 33 (2022) 385–389.
[22] Y. Lu, T. Liu, C.L. Dong, et al., Adv. Mater. 33 (2021) 2007056.
[23] W. Song, Z. Ren, S.Y. Chen, et al., ACS Appl. Mater. Interfaces 8 (2016) 20802–20813.
[24] Y. Tian, L. Cao, P. Qin, ChemCatChem 11 (2019) 4420–4426.
[25] T. Grewe, X. Deng, H. Tüysüz, Chem. Mater. 26 (2014) 3162–3168.
[26] L. Huang, D. Chen, G. Luo, et al., Adv. Mater. 31 (2019) 1901439.
[27] Q. Hu, Y. Liu, L. Ma, X. Zhang, H. Huang, J. Appl. Electrochem. 48 (2018) 1189–1195.
[28] Y. Xiong, Y. Yang, X. Feng, F.J. DiSalvo, H.D. Abruña, J. Am. Chem. Soc. 141 (2019) 4412–4421.
[29] C. Guan, W. Xiao, H. Wu, et al., Nano Energy 48 (2018) 73–80.
[30] K. Lu, T. Gu, L. Zhang, et al., Chem. Eng. J. 408 (2021) 127352.
[31] J. Zhao, W. Han, J. Zhang, Z. Tang, Arab. J. Chem. 13 (2020) 4857–4867.
[32] Y. Yang, Y. Ou, Y. Yang, et al., Nanoscale 11 (2019) 23296–23303.
[33] Y. Lu, C.L. Dong, Y.C. Huang, et al., Angew. Chem. Int. Ed. 59 (2020) 19215–19221.
[34] Z. Liu, G. Wang, X. Zhu, et al., Angew. Chem. Int. Ed. 59 (2020) 4736–4742.
[35] H.G. Cha, K.S. Choi, Nat. Chem. 7 (2015) 328–333.
[36] Y. Lu, T. Liu, Y.C. Huang, et al., ACS Catal. 12 (2022) 4242–4251.
[37] B.S. Solanki, C.V. Rode, Green Chem. 21 (2019) 6390–6406.
[38] N. Heidary, N. Kornienko, Chem. 56 (2020) 8726–8734.
[39] Y. Miao, M. Shao, Chin. J. Catal. 43 (2022) 595–610.
[40] B. Zhou, Y. Li, Y. Zou, et al., Angew. Chem. Int. Ed. 60 (2021) 22908–22914.
[41] X. Chao, C.A. Wei, A. Sd, et al., Nano Energy 71 (2020) 104653.
[42] D. Zhou, S. Wang, Y. Jia, et al., Angew. Chem. Int. Ed. 58 (2019) 736–740.
[43] H. Wang, J. Chen, Y. Lin, et al., Adv. Mater. 33 (2021) 2008422.
[44] W. Chen, C. Xie, Y. Wang, et al., Chem. 6 (2020) 2974–2993.